

ISSN 0840-8440

PROCEEDINGS

TECHNOLOGY TRANSFER CONFERENCE 1988

November 28 and 29, 1988

Royal York Hotel

Toronto, Ontario

SESSION A

AIR QUALITY RESEARCH

Sponsored by

Research and Technology Branch

Environment Ontario

Ontario, Canada

AASG

A11

**AN INVESTIGATION OF WIND GENERATED PARTICLE TRANSPORT
RATES WITHIN A TURBULENT BOUNDARY-LAYER**

A. D. Ciccone, J. G. Kowall and J. F. Keffer
Department of Mechanical Engineering
University of Toronto
Toronto, Ontario, M5S 1A4

Abstract

Most research and experiments carried out on the movement of particles in air have been concerned with the total mass transport or flux of material from a surface. It has been established that the total rate of transport can be attributed to three modes of motion which are not mutually exclusive: saltation, surface creep and suspension. Here, saltation is the most important since it is a prerequisite for the other two. The empirically determined saltation rates for wind generated particle movement are, in many cases, not in accord. Investigators have either modified the constants in Bagnold's saltation formula or developed complicated empirical equations to determine the transport rates. These equations are not likely to give further insight into the physics involved in the transport mechanisms. An alternative procedure is to examine the various components of the transport rate and determine the parameters on which it depends. A novel flow-visualization/digital image analysis technique has been developed to determine individual particle trajectories, from which saltation rates can be computed. This technique involves recording individual particle motions, which have been illuminated with a strobed light source, on 35 mm high-speed film, digitizing the film and using a high-speed computer to track the particle trajectories. The transport rates are determined subsequently from the particle-trajectory data.

Introduction

In recent years, wind generated particle transport or wind erosion has been receiving increasing attention (Barndorff-Nielsen, 1985) from scientists and engineers interested in the effects of soil erosion, snow drift, sand movement and other related natural phenomena on local environmental, agricultural and economic conditions. For example, fugitive emissions are generated from open-area sources such as coal or iron ore stockpiles by the wind. These emissions are either transported downwind, affecting the air quality of near-by air-sheds or fall out locally, acting as a hindrance to a clean work place. Wind induced erosion can also seriously affect the agricultural yield of a region, as was the case this year in the prairie provinces. In both of the above situations, valuable resources can be lost if appropriate control strategies are not adopted. In order to develop such control strategies, an understanding of the physics associated with wind erosion is required.

Previous studies (Bagnold, 1941, Chepil, 1945, Gillette, 1978) have identified three primary modes of particle transport: surface creep, suspension and saltation. Surface creep pertains to particles greater than 1000 μm in diameter, which are too heavy to

Since new estimates of asthma prevalence in children in Canada range from 10 to 20%, and possibly higher, it is clear that a substantial part of the Canadian population may be already suffering the ill effects of low-level exposure to acid gases, particularly SO₂.

(Supported by Ont. Ministry of Env't., Health & Welfare Canada)

REFERENCES

1. Mao Y; Semenciw R; Morrison H; MacWilliam L; Davies J; Wigle D. Increased rates of illness and death from asthma in Canada. *Can Med Ass J.* 1987 Oct; 137: P 620-24.
2. Esquibel KP; Foster CR; Garnier VJ; Saunders ML A program to help asthmatic students reach their potential. *Public Health Rep* 1984 Nov-Dec; 99(6): P 606-9
3. Martin AJ, McLennan LA, Lendau LI, Phelan PD. The natural history of childhood asthma to adult life. *Br Med J* 1980; 280:1397-400.
4. Blair H. Natural history of childhood asthma: 20 year follow-up. *Arch Dis Ches* 1977; 52:613-9.
5. Speight ANP, Lee DA, Hey EN. Underdiagnosis and undertreatment of asthma in childhood. *Br Med J* 1983; 286:1253-6.
6. Ellis-EF. Asthma in childhood. *J Allergy Clin Immunol* 1983 Nov; 72(5 Pt 2): P 526-39
7. Schenker MB; Samet JM; Speizer FE. Risk factors for childhood respiratory disease. The effect of host factors and home environmental exposures. *Am Rev Respir Dis* 1983 Dec; 128(6): P 1038-43
8. Ware JH; Ferris BG Jr; Dockery DW; Spengler JD; Stram DO; Speizer FE. Effects of ambient Sulfur oxides and suspended particles on respiratory health of preadolescent children. *Am Rev Respir Dis* 1986; 133: P 834-42
9. Weiss ST; Tager IB; Speizer FE; Rosner B. Persistent Wheeze: Its relation to respiratory illness, cigarette smoking, and level of pulmonary function in a population sample of children. *Am Rev Respir Dis* 1980; 122: P 697-707
10. Becklake MR; Soucie J; Gibbs GW; Ghezzi H. Respiratory health status of children in three Quebec urban communities: An epidemiologic study. *Bull Europ Physiopath Resp* 1978; 14: P 205-221
11. Fergusson DM; Horwood LJ. Parental smoking and respiratory illness during early childhood: a six-year longitudinal study. *Pediatr Pulmonol* 1985 Mar-Apr; 1(2): P 99-106
12. Halfon N; Newacheck PW. Trends in the hospitalization for acute childhood asthma, 1970-84. *Am J Public Health* 1986 Nov; 76(11): P 1308-11
13. Ware JH; Dockery DW; Spiro A III; Speizer FE; Ferris BG Jr. Passive smoking, gas cooking, and respiratory health of children living in six cities. *Am Rev Respir Dis* 1984; 129: P 366-74
14. Kerigan AT, Goldsmith CH, Pengelly LD. A three-year cohort study of the role of environmental factors in the respiratory health of children in Hamilton, Ontario. *Am Rev Respir Dis* 1986; 134:987-93.
15. Pengelly LD, CH Goldsmith, AT Kerigan, W Furlong, and SA Toplack. The Hamilton study: Effect of particle size on respiratory health in children. In: *Aerosols*; Eds. SD Lee, T Schneider, LD Grant, and PJ Verkerk; Chapter 57, pp. 753-766. Lewis Publishers, Chelsea, Mich., USA; 1986.
16. Pengelly LD, CH Goldsmith, AT Kerigan, W Furlong, and SA Toplack. The Hamilton Study: Estimating exposure to ambient suspended particles. *J. Air. Poll. Contr. Ass.* 37: 1421-1428, 1987.
17. Silverman F, P Corey, A Ayiomamitis, and HR Hosein. Health effects on asthmatics of daily variations in exposure to particulate matter. *Proc. (Ont. Min. Env't. Tech. Transfer Conf.)* A2:1-20; Toronto, ON, November 30 - December 1, 1987.

become airborne but which can roll or slide along the surface. This transport mechanism accounts for about 10% of the total mass movement. Suspension pertains to particles that generally have diameters less than 100 μm . These particles remain airborne for long periods of time and are carried along at roughly the fluid stream velocity. The dominant mass movement (about 50% to 75% of the total) occurs by saltation, which pertains to particles having diameters between 100 to 1000 μm . In this mode of transport, particles never go into complete suspension; rather, they remain close to the surface (usually within about 5 cm) forming a relatively thin "saltation layer". Within this layer the particles travel in a series of jumps or hops of about 10 cm in length. A fundamental finding of the aforementioned studies is that suspension of particles cannot occur without saltation as a prerequisite.

Investigators have basically used a mass-flux technique in which the mass uplifted from a surface is collected by a vertical array of traps and subsequently analyzed in order to develop empirical relationships for the vertical and horizontal fluxes as a function of the surface shear velocity (u_*) and other parameters. The first empirical relationship for the saltation rate (Q) was proposed by Bagnold (1941) as

$$Q = u_*^3 \quad (1)$$

This has been modified and extended (White, 1979; Gillette, 1978) to include various parameters and is the basis for most calculations to determining the erosion rate associated with a surface. Agricultural engineers have developed an empirical soil-erosion model, which involves a set of parameters, to predict the potential annual soil loss,

$$E = f(I', C', K', L', V), \quad (2)$$

where I' is the soil erodibility, C' is the local climatic factor, K' is the soil ridge roughness factor, L' is the field length and V is the vegetation factor (Chepil and Woodruff, 1963). The above equation serves to illustrate the empiricism involved in determining the erosion rate.

The mass-flux approach generally yields good engineering results for the quantity of material transported by the wind but does not provide any understanding of the physics of the wind erosion process. An approach which does so is to consider the saltation process in terms of the motion of individual saltating particles within a turbulent boundary-layer in a Lagrangian frame of reference. Such an approach has been adopted by the Turbulence Research Group (TRG) in the University of Toronto's Mechanical Engineering (UTME) Department. This involves the use of a novel flow-visualization/digital-image-analysis technique for obtaining the characteristics of individual particle trajectories. In the present work, the technique used to obtain the trajectories is described, the governing equations of motion for the particles are discussed, and results for the particle flux profiles within the saltation layer, the saltation rate and the vertical mass flux of material are presented.

Experimental Details

The acquisition of good quality images or pictures is of crucial importance in the implementation of the aforementioned technique. The elements required for this include a wind tunnel facility, a lighting system, photographic equipment and film, and a digital image data acquisition system.

Experiments were carried out in a blow-through open circuit wind tunnel located in UTME. This tunnel has a rectangular test-section (180 cm long, 31 cm wide and 61 cm high) with a plexiglass top for transmitting light and a plexiglass side for viewing. Mono-dispersed (195 μm) silica sand particle beds, 100 cm long, 10 cm wide and 0.5 cm thick, were placed along the test-section centerline. The entire test section was shrouded in black, except for a 25 cm by 25 cm viewing port located 40 cm from the leading edge of the particle bed and a 10 cm slit directly above the viewing port located along the centerline of the test section. A 35 mw He-Ne laser was used as a continuous collimated light source. The laser beam was aligned above and along the centerline of the test-section and the beam deflected 90° by a prism and passed through a cylindrical lens (4.4 cm focal length) to generate a 12 cm by 0.2 cm plane of very intense light.

Still photography was chosen in preference to high-speed cinematography, since with the former it was possible to capture most of the trajectory of an individual particle in a single frame. As a consequence, it was easier to observe the particle's path, and the amount of digitization required was reduced. In order to resolve rapid changes in particle position and velocity, the light source was "strobed" at 300 Hz by means of a rotating disk with an equal number of open and closed sectors.

A 35 mm Contax 139 SLR camera fitted with a 105 mm telephoto lens was positioned perpendicular to the flow, outside of the test-section on a tripod. The distance from the plane of the film to the plane of light was approximately 41 cm, giving a field of view of 7.5 cm by 5 cm and a depth of view of 1 mm at an aperture opening of f2.8. Kodak Recording 1000 ASA film was used as the recording medium. The camera shutter was held open for 0.5 s and, with the particles illuminated by the stroboscopic light, "dashed" particle trajectories were recorded. These enabled measurements of velocity and position to be made in a Lagrangian frame of reference.

A pitot tube was situated above the field of view to monitor the wind speed (5.5 m/s) during each experiment. Once particle motion was initiated, a roll of 36 frames, each containing a 0.5 s exposure, was shot every 2 seconds with the aid of a remote shutter cord and winder. Instantaneous wind velocity data were acquired without the particle beds present using constant temperature cross-wire hot-wire anemometers. These data were recorded and subsequently computer-analyzed to obtain the mean longitudinal and vertical velocity components, turbulent intensities, velocity spectra and Reynolds stresses.

After all the film was developed, the negatives were digitized on the UTME Digital Image Analysis System. This system has a Cohen CCD scanner with a Panasonic 25 mm T.V. lens, attached to a Quantex video processor, which is in turn connected to a micro-Vax computer. The scanner converts the image into 512 analogue scan lines which are digitized at a rate of 512 points per line by the Quantex, and the digital data are retrieved by the computer. Thus, each image is represented as a 512 by 512 matrix with each picture element or "pixel" containing 8 bits of light intensity values, giving grey-levels between 0 and 255. The digital data are subsequently stored on magnetic tape.

Image Processing and Analysis

A typical digitized image is presented in Figure 1, where the dark dashed lines on the light background represent the particle trajectories. Prior to the extraction of the dashed-line data, the images had to be enhanced to remove the noise (i.e., the uneven shades of background light and thin vertical lines due to the plexiglass) while still

maintaining the integrity of the image. Due to the large number of particles present and their various orientations, an "artificial intelligence/computer-vision" approach was needed to objectively analyse the pictorial data. Conventional approaches, such as thresholding the grey levels or their gradients (Rosenfeld and Kak, 1982), did not provide adequate image enhancement, as is evident from Figure 2. Here, a modified gradient operator was used to enhance and detect the particle lines (Ciccone et al., 1987).

A sophisticated scheme to further enhance the data was developed by considering the image as a two-dimensional signal and applying the Fourier transform to this signal. The dashed lines were found to have a particular "frequency" range which was different from that associated with the uneven background grey-level and spurious noise. A description of this scheme follows.

The two-dimensional Fourier transform of an image, a complex function with real and imaginary components, is given by:

$$F(u, v) = \iint f(x, y) e^{-j2\pi(ux+vy)} dx dy, \quad (3)$$

where F is the Fourier transform of the image f , and u and v are the image frequencies associated with the x and y directions. Since the kernel function can be separated into two parts, (3) can be carried out via two one-dimensional Fast Fourier Transforms (FFT) by first transforming the rows and then the columns of the image matrix or vice versa. Once the image has been transferred into frequency space, it can be readily filtered by means of a variety of digital filters. The "digital" representation of a band-pass filter is,

$$H(u, v) = H_h(u, v) H_l(u, v), \quad (4)$$

where $H_h(u, v)$ and $H_l(u, v)$ are the high and low pass components of the filter. The frequency-domain form of the filtered image is given by,

$$G(u, v) = F(u, v) H(u, v), \quad (5)$$

This is transformed back into the real domain via an inverse Fourier transform, i.e.,

$$g(x, y) = \iint G(u, v) e^{j2\pi(ux+vy)} du dv. \quad (6)$$

In selecting the appropriate high and low filtering frequencies, an understanding of what contributes to each domain is required. Edges and other sharp transitions in grey levels are associated with the high-frequency components while the uneven background levels contribute to the low frequency components. Thus, an image is sharpened by attenuating the low frequencies (high-pass filtering) and smoothed by attenuating the high frequencies (low-pass filtering). In the present study, a symmetrical Butterworth band-pass filter was applied to the image using 25 and 250 as the appropriate high and low cut-off frequencies. The result of applying the "Fourier" enhancement scheme is illustrated in Figure 3. As can be seen the integrity of the image is maintained, but the spurious noise has been removed and an even background of grey provided. It should be noted that this procedure is a robust and efficient means of enhancing an image.

In order to locate the particle trajectories, which are thick lines, one could use a pattern-recognition technique to compare lines of various lengths and angles with the enhanced image. This approach, however, would be extremely cumbersome and time

consuming. A more efficacious approach has been developed based on the fact that a line can be considered as a series of overlapping points, vis-à-vis the present situation. Thus, correlating the template representation of a solid circle with the image and subsequently normalizing the resulting cross-correlation function produces a series of adjacent points which represent the centers of the dashed lines. The normalized cross-correlation function (Gonzalez and Wintz, 1977) is given by:

$$C_{tg}(x, y) = \frac{\iint t(\alpha, \beta) g(x+\alpha, y+\beta) d\alpha d\beta}{[\iint t^2(\alpha, \beta) d\alpha d\beta]^{1/2} [\iint g^2(x+\alpha, y+\beta) d\alpha d\beta]^{1/2}}, \quad (7)$$

where t represents the template and g represents an image. The template used is shown in Table 1.a. Since this template also responds to vertical lines, a second template of a vertical line (Table 1.b) was cross-correlated with the image and high responses to it were ignored. Figure 4 shows the local maxima of the above cross-correlation function and, as can be seen, the dashed lines have been extracted. The computer now knows the location of each pixel but does not know the pixel-to-pixel relationship. These pixels form a set of candidate points to be arranged into subsets which make up lines of finite length. Similarly, these subsets form the particle trajectories which must be linked together. This line tracking analysis can be considered a type of artificial intelligence/computer-vision analysis.

Initially, the candidate pixels are extracted from the digitized image column by column, i.e., all candidates in column 1 followed by all candidates in column 2, etc. The following three tracking criteria are used: (i) the nearest neighbour (i.e., Euclidean) distance $\leq \sqrt{2}$; (ii) a minimum number of pixels is required to form a line; (iii) the pixels form a line which has no curvature. Criterion (i) is used to either initiate a line or to extend a line which is being tracked; (ii) is used to rid the image of residual noise; (iii) is used to break up lines which either cross or make sudden deviations, as is the case when a particle rises from or impacts upon a surface. This process is a combined parallel and serial approach where more than one line is followed at any one time. Note that when lines cross, they are flagged and any pixel which is accepted for one line is cross-checked with other line to see if it may belong to both lines. The line subsets are then used to link the line segments together and reconstruct the trajectories. Figure 5 shows a typical result of applying the procedure.

Since the light source was strobed at a 300 Hz, each particle trajectory was divided into small straight line segments, with adjacent segments having similar characteristics, i.e., direction of flight and length. Thus, the difference in characteristics between dashed lines which belong to the same trajectory should be small. The line segments are linked together by first extending a given line by its own length in its direction of flight from left to right, i.e., the "end" coordinates of the extended line are given by:

$$x_{\text{end}} = x_2 + \Delta x \quad (8.a)$$

$$\text{and } y_{\text{end}} = y_2 + \Delta y, \quad (8.b)$$

where x_2 and y_2 are the end coordinates of the original line of length $\Delta l = (\Delta x^2 + \Delta y^2)^{1/2}$. Lines are linked together using the following three criteria: (i) the product of the slopes of any two lines must be positive or zero; (ii) the difference between the start of a candidate line and the end of the extended line must be less than a specified threshold; (iii) the

size of the lines must be similar. The first criterion is used to ensure that the lines are collinear and the second and third are used to ensure that they belong to the same particle path. The result of using these criteria is presented in Figure 6. Note that the particle velocities are obtained by multiplying the length of the line segments by the strobing frequency. As illustrated, the particle trajectories are incomplete. In order to complete the trajectories, a Lagrangian random-flight model, based on the particles' equations of motion is used.

Lagrangian Random-Flight Model

In the present case, the particles can be considered spherical, and the requisite equation of motion can be derived from a force balance on an individual particle as follows. Newton's second law yields:

$$m_p \frac{d\vec{V}_p}{dt} = \sum \vec{F}_i, \quad (9)$$

where m_p is the particle mass, \vec{V}_p is the particle velocity and $\sum \vec{F}_i$ is the sum of the relevant forces comprising drag, lift, pressure, gravity and virtual mass as given below.

$$\vec{F}_{drag} = -C_d \frac{\pi}{4} D^2 \rho_f \frac{|\vec{V}_R| |\vec{V}_R|}{2} \quad (9.a)$$

$$\vec{F}_{lift} = -C_l \frac{\pi}{6} D^3 \rho_f (\vec{V}_R \times \vec{\Omega}) \quad (9.b)$$

$$\vec{F}_{pressure} = \frac{\pi}{6} D^3 \rho_f \frac{d\vec{V}_f}{dt} \quad (9.c)$$

$$\vec{F}_{gravity} = -(\rho_p - \rho_f) \vec{g} \quad (9.d)$$

$$\vec{F}_{virtual\ mass} = C_{vm} \frac{\pi}{6} D^3 \rho_f \left[\frac{d\vec{V}_f}{dt} - \frac{d\vec{V}_p}{dt} \right] \quad (9.e)$$

In equations (9.a) to (9.e), C_d , C_l and C_{vm} are the coefficients of drag, lift and virtual mass, respectively, \vec{g} is gravity, D is the particle diameter, ρ_p and ρ_f are the particle and fluid densities and \vec{V}_R is the particle relative velocity given by:

$$\vec{V}_R = (\vec{V}_{xR}^2 + \vec{V}_{yR}^2)^{1/2}, \quad (10)$$

with

$$\vec{V}_{xR} = \vec{V}_{xp} - \vec{U}, \quad (10.a)$$

$$\vec{V}_{yR} = \vec{V}_{yp} - \vec{V}, \quad (10.b)$$

where \vec{U} and \vec{V} are the components of the fluid velocity (\vec{V}_f) in the x and y directions, respectively.

After substitution and rearrangement, the resulting equation is

$$\left(\frac{\rho_p}{\rho_f} + C_{vm} \right) \frac{d\vec{V}_p}{dt} = -\frac{3}{4} C_d \frac{|\vec{V}_R| |\vec{V}_R|}{D} + \left(1 + C_{vm} \right) \frac{d\vec{V}_f}{dt} + \left[\frac{\rho_p}{\rho_f} - 1 \right] \vec{g} - C_l (\vec{V}_R \times \vec{\Omega}). \quad (11)$$

Since $\rho_p \gg \rho_f$ the above equation can be reduced to the following, with only the drag, lift and gravity forces being retained:

$$\frac{d\vec{V}_p}{dt} = -\frac{3}{4} C_d \frac{\rho_f}{\rho_p} \frac{|\vec{V}_R| |\vec{V}_R|}{D} - C_l \frac{\rho_f}{\rho_p} (\vec{V}_R \times \vec{\Omega}) - \vec{g}. \quad (12)$$

This equation provides a Lagrangian description of the particle path. The drag coefficient C_d varies with the particle Reynolds number

$$Re_p = \frac{|\vec{V}_R| D}{\nu}, \quad (13)$$

and is calculated from empirical relationships (Morsi and Alexander, 1972). The lift force is given in terms of the vector product of the relative particle velocity and the fluid vorticity,

$$\vec{\Omega} = \nabla \times \vec{V}_f, \quad (14)$$

and was considered by Hunt et al. (1984). This force is similar to the lift force which acts on an airfoil in an inviscid flow with circulation.

Given an initial particle velocity and position and the wind field, (12) can be integrated numerically, both forward and backward in time, to determine the particle impact and ejection points and velocities. By randomly varying the wind field components and ensemble averaging the trajectories, a stochastic description of the particle's trajectory can be realised. Using the wind field measured by the hot-wire anemometers, the trajectories are completed as shown in Figure 7. It should be noted, that the fluid has been assumed to be unaffected by the presences of the particles.

Approximately 100 trajectories were recorded and analyzed to determine various physical characteristics such as the particle ejection velocity vector, maximum height and jump length. These trajectories are consistent with those described by Owen (1964), White and Schulz (1977) and Hunt and Nalpanis (1985). A synopsis of the 195 μm particle results for a 5.5 m/s wind are presented in Table 2. From the latter, it is apparent that the mean ejection velocities are greater than both u_* and the fluid threshold velocity (u_{*c}). This would indicate a mechanism other than mean shear stress acts to eject particles in to the boundary-layer. The most likely mechanism is impaction from other particles rather than the lift force generated by the wind shear, since this force corresponds to less than 6% of gravity.

Estimation of the Mass Movement

With the aid of the actual trajectories, estimates of the particle fluxes, concentrations and saltation rates can be made, i.e. Lagrangian data can be used to obtain Eulerian point data. On the assumption that saltation is uniform and stationary, the mass flux of particles across unit width of a plane perpendicular to the fluid stream is

$$G(D) = \int_0^{y^*} m \chi V_{xp} dy, \quad (15)$$

where G is the saltation rate, χ is the particle concentration, m is the mass of a particle of diameter D , V_{xp} is the particle horizontal velocity and y^* is the height of the trajectory traced out by the particle (Owen, 1964). The integrand represents the horizontal flux of material. Now, (15) can be rewritten as,

$$G(D) = m \phi(D) \int_0^{t^*} \bar{x}(t;D) dt \quad (16)$$

where $\phi(D)$ is the vertical flux of particles, $\bar{x}(t;D)$ is the particle horizontal velocity as a function of time and t^* is the time of travel. This results in:

$$G(D) = m \phi(D) \bar{x}(D), \quad (17)$$

where $\bar{x}(D)$ is the particle jump length (Jensen and Sorensen, 1982).

Evaluation of (15) and (17) using the calculated particle trajectories is carried out by recording the number of particles caught in an ideal "numerical trap" and their horizontal velocities. This trap is unit width, Δy units high and is located at the maximum height of a particle trajectory. The horizontal flux of particles is determined at each trap height, and from this, the saltation rate is calculated using (15). Also, since the mean particle jump length is known, the vertical flux is calculated from (17).

In order to obtain stable concentration and flux profiles, the ejection velocity components of each particle are varied several times, using a Gaussian random number generator, particle jump lengths are determined and particle data are ensemble-averaged until convergence is attained. It was found that repeating the procedure (i.e., varying the velocity components) 500 times provided adequate convergence. Figure 8 presents the normalized horizontal fluxes as a function of height obtained for the 195 μm particles. The saltation rate was calculated to be 0.124 g/cm/s using (15) and the vertical suspension rate was calculated to be 0.017 g/cm²/s using (17). It is noted that the trend of the present results is similar to that of the data presented by Hunt and Nalpanis (1985).

Conclusions

Flow-Visualization of saltating silica-sand particles in a wind-generated boundary-layer has been achieved. The resulting particle-trajectory data have been objectively analyzed using an artificial intelligence/computer-vision approach. A two-dimensional Lagrangian model has been developed and implemented to complete the particle trajectories and from this, the mass flux of material has been estimated.

The particle statistics indicate that impacting particles have a substantial effect on the ejection of other particles since the particle ejection velocities are greater than the surface friction velocity. But, as suggested by Owen (1964), the introduction of particles

into the fluid boundary-layer results in a slowing down of the fluid velocity, since the particles act as momentum sinks; thus, particles that are subsequently ejected do not gain as much momentum. It is suggested that the fluid boundary-layer acts as a feed back mechanism.

A hypothetical scenario for the saltation process would be as follows.

- (i) Initial particles begin to saltate when the wind exceeds the particles fluid threshold velocity.
- (ii) Particles gain momentum from the boundary layer and impact onto the surface; the boundary-layer adjusts itself due to this exchange of momentum.
- (iii) Impacting particles transfer momentum to the surface, in addition to that transferred via the boundary-layer.
- (iv) The momentum transmitted to the surface is partitioned between the impacting particles which continue to saltate and other particles causing them to eject.
- (v) Steps (ii) to (iv) are repeated until a steady-state condition is reached.

Acknowledgements

This research was supported by the Ontario Ministry of the Environment, Grant 372G.

References

- [1] Bagnold, R.A., 1941: *The Physics of Blown Sand and Desert Dunes*, Methuen and Co. Ltd., London.
- [2] Barndorff-Nielsen, O.E., Muller, J.T., Remer Rasmussen, K. and Willetts, B.B., 1985: eds., *Int. Workshop on Physics of Blown Sand*, Univ. of Aarhus, May.
- [3] Chepil, W.S., 1945: Dynamics of Wind Erosion: I, Nature of Movement of Soil by Wind, *Soil Science*, 60, 305-320.
- [4] Chepil, W.S. and Woodruff, N.P., 1963: The Physics of Wind Erosion and its Control, *Advances in Agronomy*, Academic Press, Toronto, 15, 1-301.
- [5] Ciccone, A.D., Kawall, J.G. and Keffer, J.F., 1987: Digital Image Analysis of Macroscopic Particle Motions Generated by a Turbulent Wind, *Sixth Symposium on Turbulent Shear Flows*, Toulouse.
- [6] Gillette, D., 1977: Fine Particulate Emissions Due to Wind Erosion, *Trans. ASAE*, 890-897.
- [7] Gonzalez, R.C. and Wintz, P., 1977: *Digital Image Processing*, Addison-Wesley, Massachusetts.
- [8] Hunt, J.C.R. and Nalpanis, P., 1985: Saltation and Suspended Particles over flat and Sloping Surfaces, *Proc. Int. Workshop on Phys. of Blown Sand*, Aarhus.
- [9] Hunt, J.C.R., Thomas, N.H., Auton T.R. and Sene, K., 1984: Entrapment and Transport of Bubbles by Plunging Water, *Gas Transfer at Water Surfaces*, eds. Wilfried Brutsaert and Gerhard H. Jirka, D. Reidel Publishing, Boston, 255-268.

- [10] Jensen, J.L. and Sorensen, M., 1982: On Mathematical Modeling of Aeolian Saltation, *Euromech 156*, Istanbul.
- [11] Morsi, S.A. and Alexander, A.J., 1972: An Investigation of Particle Trajectories in Two-Phase Flow Systems, *J. Fluid Mechanics*, 55, 193-208.
- [12] Owen, P.R., 1964: Saltation of Uniform Grains in Air, *J. Fluid Mechanics*, 20, 225-242.
- [13] Phillips, C.J. and Willetts B.B., 1978: A Review of Selected Literature on Sand Stabilization, *Coastal Engineering*, 2, 133-147.
- [14] Rosenfeld, A. and Kak, A.C., 1982: *Digital Image Processing*, Vol 2, Academic Press, Toronto.
- [15] Rubinow, S.I. and Keller, J.B., 1961: The Transverse Force on a Spinning Sphere Moving in a Viscous Fluid, *J. Fluid Mechanics*, 11, 447-459.
- [16] White, B. R., 1982: Two-Phase Measurements of Saltating Turbulent Boundary-Layer Flow, *Int. J. Multiphase Flow*, 8, 459-473.
- [17] White, B.R. and Schulz, J.C., 1977: Magnus Effect in Saltation, *J. Fluid Mechanics*, 83, 497-512.

Table 1.a Template representation of a solid circle used in template matching with image.

	-1	-1	-1	-1	-1	-1	-1
	-1	-1	0.7	1	0.7	-1	-1
	-1	0.7	1	1	1	0.7	-1
$t(\alpha, \beta) =$	-1	1	1	1	1	1	-1
	-1	0.7	1	1	1	0.7	-1
	-1	-1	0.7	1	0.7	-1	-1
	-1	-1	-1	-1	-1	-1	-1

Table 1.b Template representation of a vertical line used in template matching with image.

	-1	-1	1	1	1	-1	-1
	-1	-1	1	1	1	-1	-1
	-1	-1	1	1	1	-1	-1
$t(\alpha, \beta) =$	-1	-1	1	1	1	-1	-1
	-1	-1	1	1	1	-1	-1
	-1	-1	1	1	1	-1	-1
	-1	-1	1	1	1	-1	-1

Table 2. Mean trajectory characteristics for 195 μm particles

Mean wind velocity	(U)	5.5 m/s			
Surface friction velocity	(u_*)	25 cm/s			
Threshold friction velocity	(u_{*c})	29 cm/s			
		Ejection		Impact	
		Mean	Std Dev	Mean	Std Dev
V_{xp}	(cm/s)	5.4	6.8	134.	6.2
V_{yp}	(cm/s)	38.	1.8	-32.	1.6
V_p	(cm/s)	49.0	7.2	138.	6.4
Angle	(deg)	74.	36.	-13.0	3.0
V_p/u_*		1.9		5.5	
Height _{max}	(cm)	0.86	0.7		
Length	(cm)	7.2	5.5		
Height/Length		0.12			
No. of trajectories		123			

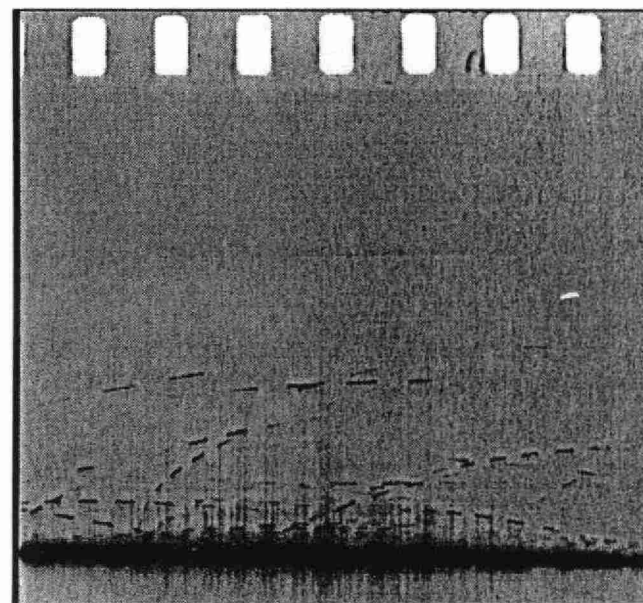


Figure 1 Digitized negative of 195 μm particles moving left to right.

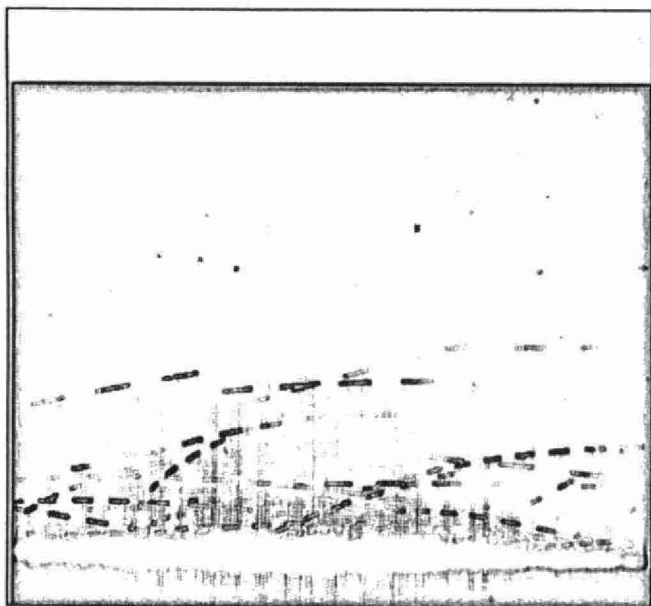


Figure 2 Sobel gradient operator applied to image.

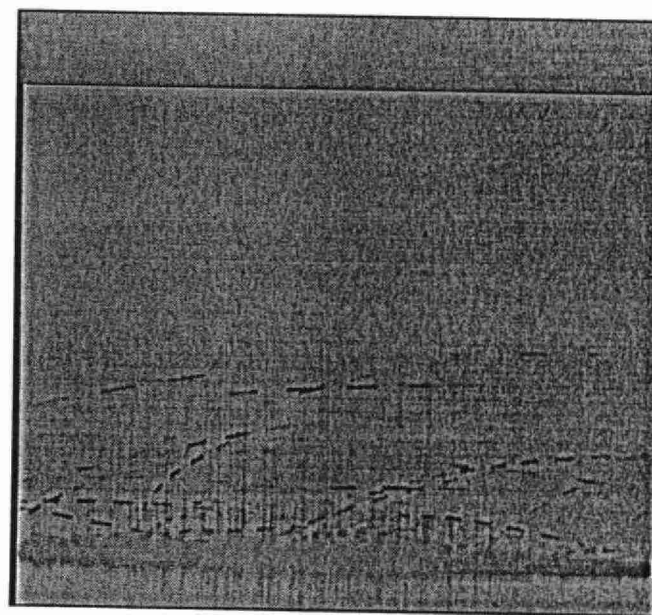


Figure 3 Fourier enhancement of raw image using a Butterworth band pass filter (25 to 250).

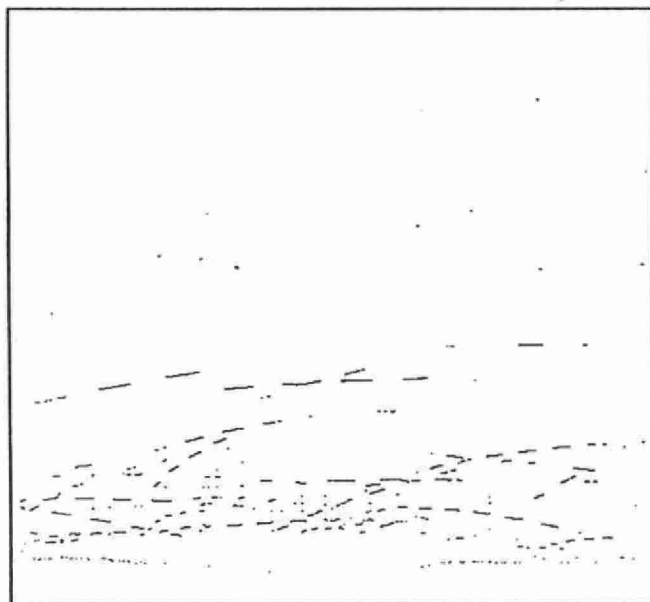


Figure 4 Image after applying template matching to enhanced image.

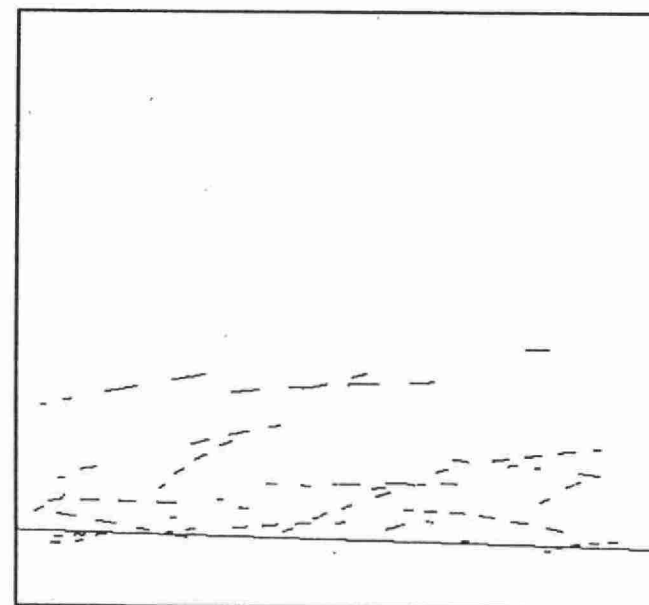


Figure 5 Results after applying line tracking procedure.

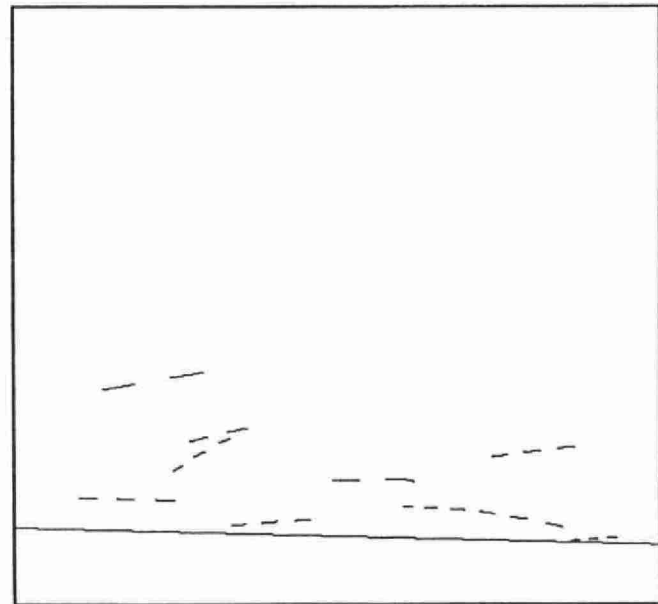


Figure 6 Results after applying line tracing routine.

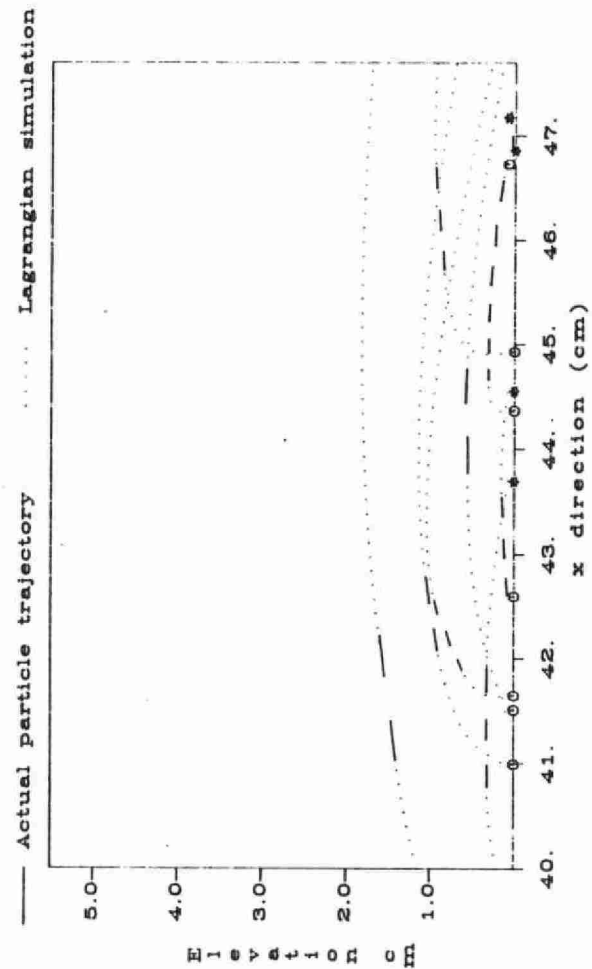


Figure 7 Reconstruction of $195\text{ }\mu\text{m}$ particle trajectories in a 5.5 m/s wind and a 25 cm/s friction velocity.

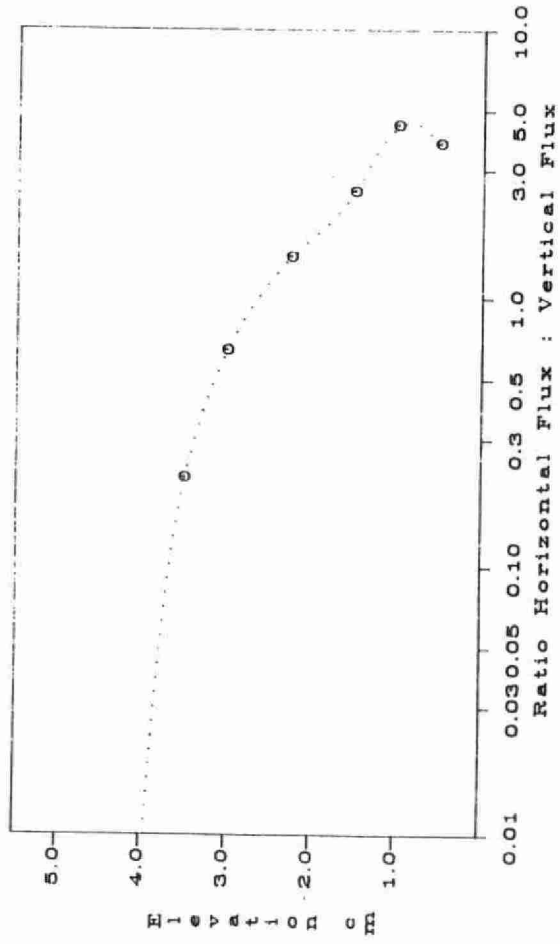


Figure 8 Ratio of Horizontal to Vertical flux for 195 μm particles under a 25 cm/s friction velocity.